



Cyclic strain in human carotid bifurcation and its potential correlation to atherogenesis: Idealized and anatomically-realistic models

M.R. KAAZEMPUR-MOFRAD¹, H.F. YOUNIS¹, S. PATEL¹, A. ISASI¹, C. CHUNG¹, R.C. CHAN², D.P. HINTON², R.T. LEE³ and R.D. KAMM^{1,*}

¹Department of Mechanical Engineering and Division of Biological Engineering, Massachusetts Institute of Technology, Cambridge, MA, U.S.A.; ²Department of Radiology, Massachusetts General Hospital, Harvard Medical School, Boston, MA, U.S.A.; ³Cardiovascular Division, Brigham and Women's Hospital, Harvard Medical School, Boston, MA, U.S.A.

Received 30 September 2002; accepted in revised form 22 August 2003

Abstract. Various mechanical phenomena are thought to contribute to the pathogenesis of atherosclerosis. Most finite-element analyses of arterial-wall mechanics to date have focused on the quantification of mechanical wall stresses, despite an abundance of experimental evidence suggesting that endothelial and smooth muscle cells readily respond to cyclic strain. In this study, we calculate the physiologic cyclic strains in the carotid bifurcation, a common site of disease. Several geometries are constructed in this study, namely (i) a 3-D, but idealized geometry of the human carotid bifurcation, (ii) 3-D subject-specific geometries based on *in vivo* images of healthy volunteers' carotid bifurcations, and (iii) 2-D models based on histology-derived patient-specific anatomy and intra-plaque components. Results in both types of 3-D model show that the highest variations in cyclic strain are found at the adjoining wall of the external-common carotid and at the carotid apex, both frequent sites of early inflammation, as well as immediately distal to the carotid bulb, a site of late-stage disease, suggesting that cyclic strain may play a role in inflammation in that region as well. The 2-D models of diseased arteries show generally muted cyclic strain, but also regions such as in the shoulder regions of a fibrous cap adjacent to a lipid pool where cyclic strains are considerably elevated.

Key words: atherosclerosis, cyclic strain, finite-element analysis, endothelial-cell proliferation, leaky junctions

1. Introduction

Considerable evidence points to the potential role of cyclic strain in regulating the function of endothelial (ECs) and vascular smooth muscle cells (SMCs). Monocyte chemoattractant protein-1 (MCP-1), significant for its involvement in monocyte recruitment into the arterial wall and atherosclerotic lesions [1] is synthesized by both ECs and vascular SMCs subjected to mechanical deformation. MCP-1 mRNA expression in rat aortic SMCs has been shown to increase *in vitro* in response to mechanical deformation as well as *in vivo* in hypertensive rats [2,3]. ECs have also been shown to exhibit similar gene expression patterns in response to cyclic strain [4,5].

Cyclic strain has also been shown to have numerous other effects on endothelial and smooth muscle cells. It stimulates vascular SMCs to release fibroblast growth factor-2 (FGF-2) in culture [6], which plays a role in early SMC migratory and proliferative responses following

*To whom correspondence should be addressed. 77 Massachusetts Avenue, Room NE 47-321, Cambridge, MA 02139, U.S.A. E-mail: rdkamm@mit.edu

arterial injury [7] and has mitogenic effects on ECs and SMCs [8–10]. Additionally, Lee *et al.* [11] have shown that versican, a vascular SMC proteoglycan that accumulates during atherosclerosis [12] and binds low-density lipoprotein cholesterol (LDLs), is induced by 4% cyclic strain. Cyclic strain has also been shown to increase EC proliferation, as demonstrated by Li *et al.* [13] who established that there exists an optimal cyclic strain range for EC proliferation ($< 6.4\%$), which if exceeded dampens the proliferative response.

EC mitosis has frequently been implicated as a mechanism for increasing the permeability of the arterial wall. Weinbaum *et al.* [14] were the first to propose the ‘leaky-cell-junction hypothesis’ in which transient pores resulting from ‘leaky’ junctions in cell turnover provide the primary trans-endothelial pathway for LDLs. Experimentally, it has been shown that aortic ECs in mitosis indeed exhibit enhanced macromolecular permeability [15,16]. Since cyclic strain plays a role in EC mitosis, it is possible that there exists a correlation between high cyclic strain levels and enhanced macromolecular permeability, in turn leading to atherosclerotic inflammation. This is further supported by the work of Tropea *et al.* [17], who have shown that reduction of aortic wall motion (using an external, stiff wrap) in the rabbit inhibits experimentally induced atherosclerosis.

It has been extensively demonstrated that low/oscillatory fluid shear stress correlates well with some commonly diseased sites in the arterial tree, such as the carotid bulb (see *e.g.* [17,18]), but the low-shear-stress hypothesis has failed to explain the prevalence of atherosclerotic inflammation/intimal thickening as observed by several researchers in other sites, such as the inner wall of the external carotid artery [20] and flow dividers [21], a high-shear-stress region.

Despite the growing body of evidence that cyclic strain may be a critical factor in early disease, most previous numerical studies using finite-element analysis (FEA) models of arterial-wall mechanics have focused on the quantification of mechanical wall stresses rather than strains [22,23].

In this study, we use finite-element models to aid in understanding the biomechanical factors that promote early inflammation in the arterial wall with emphasis on cyclic strain in the carotid bifurcation, a commonly diseased site of the cerebral circulation.

2. Methods and model description

Several geometries were utilized in this study, namely: (i) a 3-D but idealized geometry to represent general features of human carotid bifurcations (ii) three different 3-D subject-specific anatomically realistic geometries based on *in vivo* images of healthy volunteers, in order to investigate the role of detailed anatomical features specific to different human subjects, and finally (iii) several 2-D models created based on histology-derived patient-specific anatomy and intra-plaque components, in order to study the effect of arterial inhomogeneous morphology and composition on cyclic strain patterns.

The materials and methods utilized in each of these three classes of models are described below.

2.1. THE 3-D IDEALIZED MODEL

The geometry of the idealized model was created based on the work of Bharadvaj *et al.* [24] and Delfino [25]. The solid model was made in SolidWorks (SolidWorks Corporation, Concord, MA) and imported into the finite-element software for meshing and analysis. Only

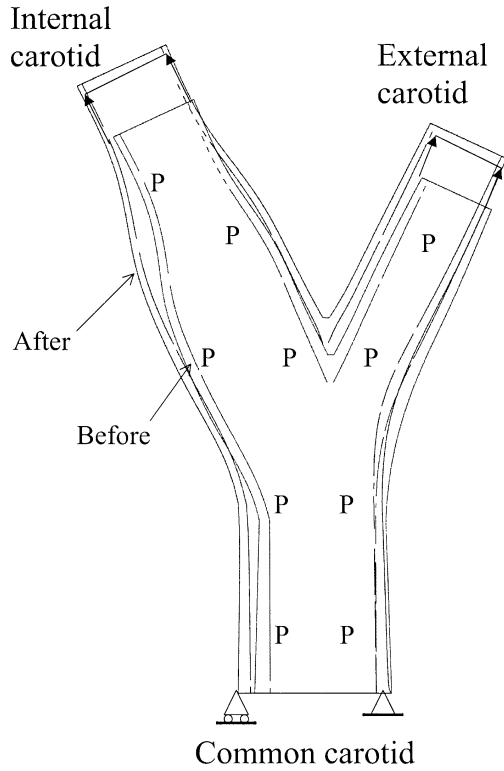


Figure 1. Solid model used for the arterial wall. “P” represents the inner surfaces, where the pressure boundary condition was applied. The solid arrows represent an applied axial strain of 10%. The pressure was ramped from 0 mmHg through 80 mmHg (diastole) to 120 mmHg (systole) and the results saved at diastole and systole.

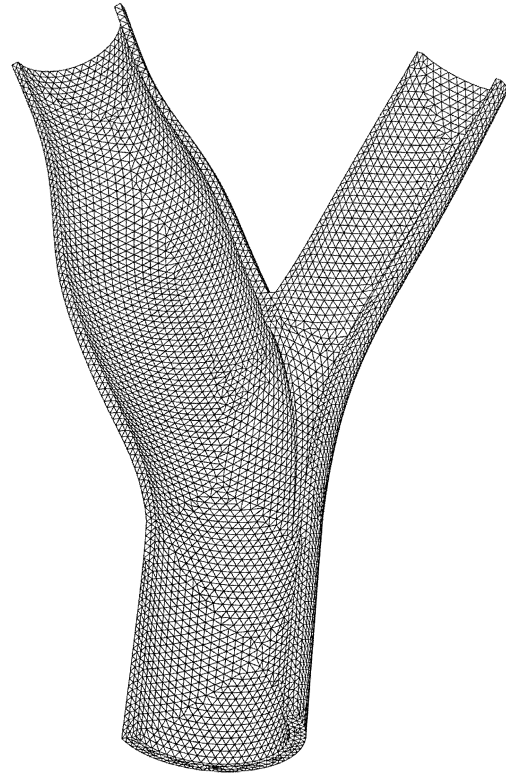


Figure 2. Computational mesh used in simulations. Half the bifurcation was modeled by making use of symmetry.

half of the geometry was modeled, exploiting the geometrical symmetry of the model. The model geometry and boundary and loading conditions are illustrated in Figure 1.

The arterial solid response was modeled using the standard Lagrangian formulation for large displacements and large strains [26, Chapter 6]. An isotropic form of the strain-energy density function for the (nearly) incompressible artery wall is specified as [22]:

$$W = \frac{a}{b} \left(e^{\frac{b}{2}(I_1-3)} - 1 \right) \quad (1)$$

where a and b ($a = 44.25$ kPa, $b = 16.73$) are elastic constants that reflect the elastic properties and tissue composition; I_1 is the first invariant of the strain tensor. In the Taylor-series expansion, a has the significance of the elastic modulus. This exponential form is appropriate for arterial mechanics since it portrays the well-known strain-stiffening behavior of collagen.

The maximum variation in pressure along a healthy carotid bifurcation (primarily due to inertial and curvature effects) is normally less than 5% of the systolic pressure [27]. This, in addition to the fact that the arterial-wall behaves in a pseudoelastic (*i.e.*, with negligible

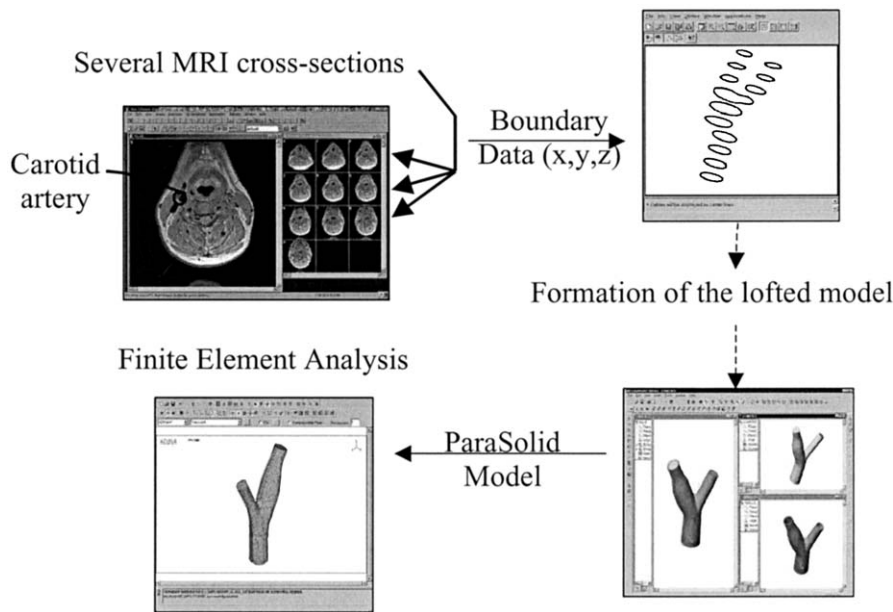


Figure 3. Procedure used to import MRI image data from source into finite-element package. Note that both fluid and solid domains are generated.

viscoelasticity) manner [28], motivated us to perform static inflation of the arterial wall models to examine the strain levels experienced within the bifurcation. An axial stretch of 10% was applied to the solid domain, as measured *in situ* by Delfino [25] who found that carotid arteries shortened by approximately 10% after excision. The arterial wall was meshed using unstructured grids (Figure 2) with 43,334 eleven-node quadratic 3-D tetrahedral solid elements, producing 118,229 nodes. The internal pressure was incrementally ramped from 0 mmHg to 80 mmHg (diastole) and subsequently to 120 mmHg (systole).

2.2. THREE-DIMENSIONAL REALISTIC GEOMETRIES

Three anatomically realistic models were created based on the *in vivo* imaging of the carotid bifurcation in healthy normal volunteers (NV) in the age range of 24–30 years. These geometries are presented here as characteristic examples of typical variations that arise between healthy volunteers. The procedure for the processing of each healthy volunteer's data is composed of several stages: magnetic resonance (MR) imaging, edge detection, lofting, flow-profile generation and finally, finite-element analysis. Acquisition of MR geometry is achieved using a surface coil that matches the jawline just above the carotid bifurcation. The edge detection protocol reads the geometry MR data to generate a series of 2-D slices. The 3-D vascular structure is reconstructed using a solid modeling software package Solidworks, by lofting across the 2-D cross-sectional structures of each level of the carotid bifurcation. An overall schematic of this process is illustrated in Figure 3, and further details of this procedure are described in [27]. In particular, the procedure for reconstruction of the apical region was as follows: The first step was the interpolation through the contours of the common carotid artery (CCA) and the internal carotid artery (ICA), skipping the 'figure eight' curves of the bifurcation region itself, using a loft function from Solidworks, building one 'branch' volume. Subsequently, a second loft function was used to interpolate through the curves of the CCA

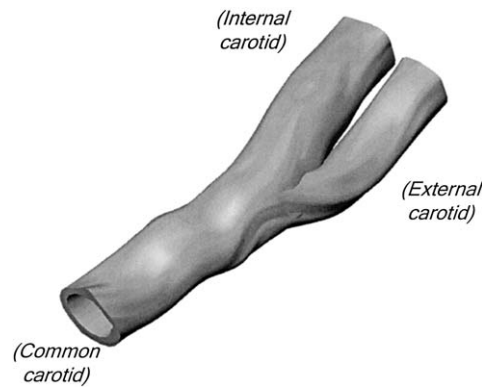


Figure 4. A typical lofted wall geometry based on MR data.

and the external carotid artery (ECA), again skipping the ‘figure eight’ curves, building a second ‘branch’ volume. These two volumes were then merged using the ‘merge’ function in Solidworks, yielding the carotid bifurcation volume. This reconstruction was performed in this manner to avoid interpolating directly through the ‘figure eight’ contours at the levels comprising the bifurcation region itself, which would result in sharp edges, discontinuities and other artifacts not compatible with healthy anatomy. Hence, the reconstruction of the apical region of the carotid bifurcation rests on the assumption of axial continuity in the curvature and overall smoothness of the vessel, which seems a reasonable assumption in the case of healthy volunteers. Each reconstructed geometry was compared to several axial MRI images of the carotid bifurcation, to ensure that the reconstructed volume was in agreement with each particular volunteer’s bifurcation anatomy.

The geometry of NV1 is presented in Figure 4. An axial stretch of 10% was applied to the solid domain (the MRI reconstructed models were first shrunk uniformly by 10% to simulate the *ex-vivo* load-free state, as suggested by Delfino [25]; this compensated for the distensibility due to blood pressure as well as the axial pre-stretch). Eleven-node quadratic elements were used to mesh the wall domain. Grid-sensitivity analysis was performed on each model to ensure independence of the solution from spatial discretization. The mesh convergence criterion was set 0.5% maximum difference in the magnitude of cyclic strain between the two finest computational grids. The final meshes contained, respectively for realistic models NV1 to NV3, 75,076 elements with 99,049 nodes, 124,992 elements with 326,610 nodes, and 74,275 elements with 197,258 nodes.

As in the idealized model (see Section 2.1), the arterial solid response was modeled using the standard Lagrangian formulation for large displacements and large strains with an isotropic form of the strain energy density function for the (nearly) incompressible artery wall [22]. The pressure was ramped incrementally from zero to subject-specific diastolic pressure, and then to subject-specific systolic pressure. The corresponding systolic/diastolic pressures were 112/58, 100/58, and 105/80 mmHg for realistic models of NV1 to NV3, respectively.

2.3. TWO-DIMENSIONAL HISTOLOGY-DERIVED MODELS

Four specimens were analyzed, which contained different combinations of lipid pool, arterial wall, fibrous plaque, and calcification. 2-D patient-specific geometries were created based on histology specimens (advanced plaques) harvested from three patients after carotid endarterectomy (Figure 5). During the endarterectomy, the atherosclerotic plaques were excised, sliced,

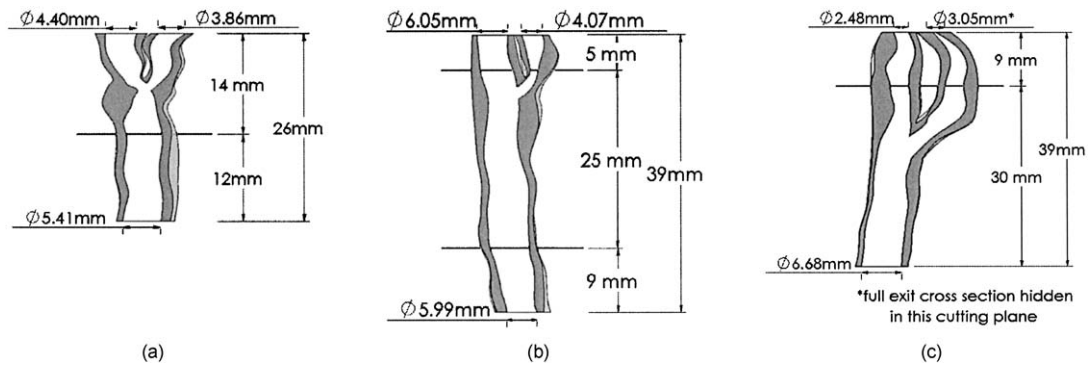


Figure 5. Schematics of patient models and the location of histology slices.

and stained for lipid, collagen, smooth muscle cells, and macrophages. By taking a digitized picture of each stained slice, the plaque composition could be determined and used to construct a 2-D replica of the slice using finite-element methods. It must be remarked that our 2-D finite-element analyses were conducted using the plane-strain assumption. This assumption is valid if the vessel is either constrained longitudinally or if the longitudinal dimension is sufficiently large so that longitudinal strains are negligible, which may not necessarily be the case *in vivo*. Thus, analysis of 3D plaque geometry can provide a more complete and more accurate representation of the plaque biomechanics. A similar 3-D reconstruction based on histology specimens would require a large number of histology slides, which would be prohibitively expensive and time consuming.

The model shown in Figure 6a corresponds to the slice shown in patient geometry of Figure 5a, on mid common carotid artery. Models in Figures 6b and 6c, correspond, respectively, to the top and bottom slices shown in the patient geometry of Figure 5b, the former being a slice through the proximal internal carotid just upstream of the carotid bulb and downstream of a stenosis, and the latter corresponding to proximal common carotid artery. Finally, the model shown in Figure 6d is from the histology slice in the patient model of Figure 5c, and corresponds to the proximal internal carotid just downstream of a stenosis.

Each 2-D model was divided into regions of lipid, arterial wall, and fibrous plaque, and calcification, if applicable. Fibrous plaque was assumed to be any region other than lipid, arterial wall, and calcified areas. Specifically, in this model fibrous plaque consisted of macrophages, SMCs and collagen, in accordance with the fact that SMCs, collagen and macrophages often coexist in many areas. Since SMCs secrete collagen [29], both stains overlap in many regions. The macrophage-infested areas were also found, during histology processing, to coincide with some regions of smooth muscle cells and collagen, particularly in the regions surrounding the lipid pools and the fibrous cap.

Nine-node plain strain elements were used to mesh these models. A typical mesh (see model of Figure 6b) contained 11,769, of which 3,583 were arterial wall, 489 were lipid, and 7,697 were fibrous plaque. Each of the three regions was modeled as a rubber-like material, defined using Mooney-Rivlin parameters. Mooney-Rivlin materials can be described using two constants, $D_1 = a/b$ and $D_2 = b/2$, where a and b , the coefficients for the strain-energy-density function are defined in Equation (1). D_1 is proportional to the elastic modulus at zero strain, and D_2 characterizes the elastic sensitivity of the material to increasing stress. For arterial wall, the Mooney-Rivlin parameters were taken from a previous study, which concluded $D_1 = 2644.7$ Pa and $D_2 = 8.365$ [22]. The lipid parameters of $D_1 = 50$ Pa and

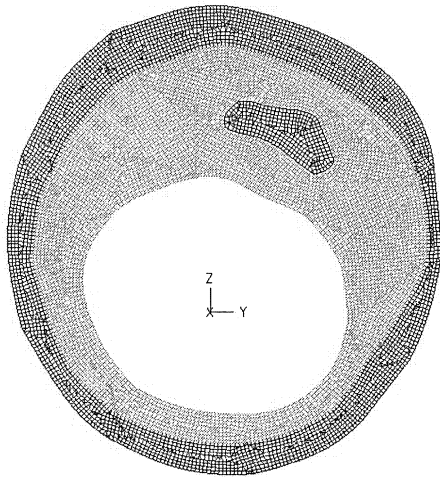


Figure 6-a

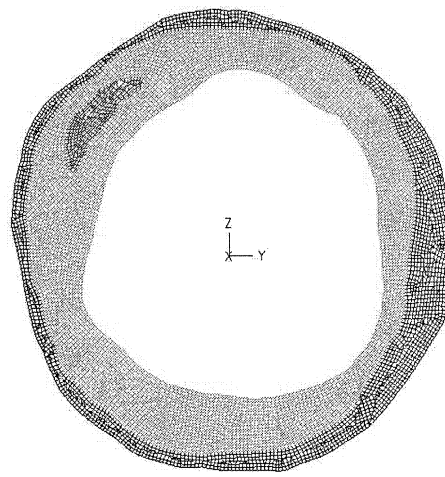


Figure 6-b

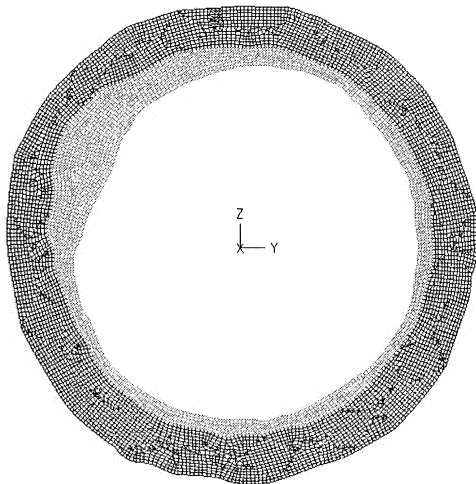


Figure 6-c

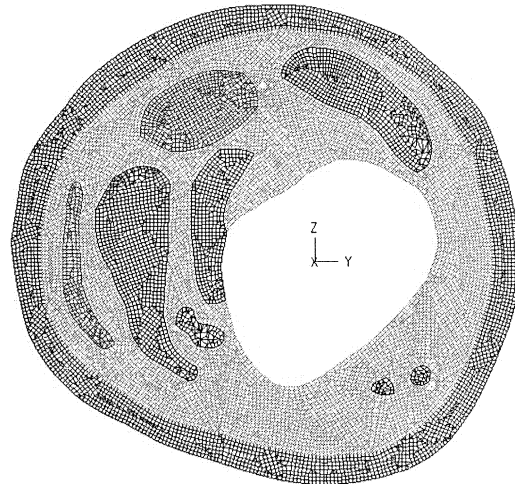


Figure 6-d

Figure 6. Finite-element meshes in 2-D histology-derived models. Different colors indicate different composition materials. Namely, colors black, red, light and dark blue denote calcification, lipid, fibrous plaque, and arterial wall, respectively.

$D_2 = 5$ were taken from studies of mechanical properties of lipid that is normally found in the atheroma [30]. For fibrous plaque, $D_1 = 5105.3$ Pa and $D_2 = 13$, found from a study which provided uni-axial test data of human atheroma [31].

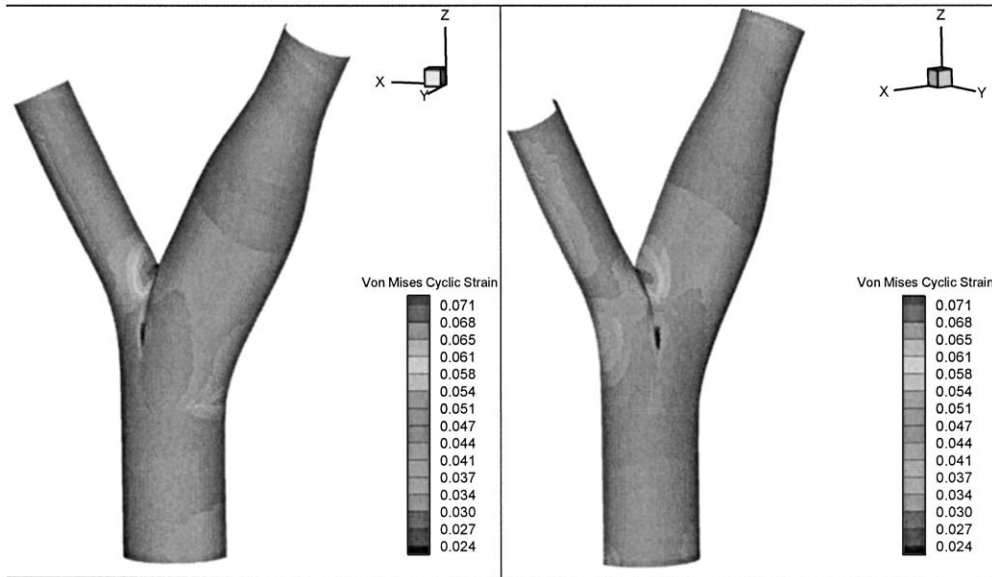


Figure 7. Bandplot of Von Mises cyclic strain. Note the areas of elevated ($\sim 6\text{--}7\%$) strain, namely the external carotid wall opposite the flow divider, the flow divider itself and immediately distal to the carotid bulb.

3. Finite-element analysis

A commercial finite-element analysis program (ADINA, version 7.4, Automatic Dynamic Incremental Nonlinear Analysis, Watertown, MA) was employed to carry out solid mechanic simulations using the geometries described above. The solutions were stored only at systole and diastole and the Von Mises cyclic strain was computed as the difference between these two states:

$$\varepsilon_{VM,cyclic} = \varepsilon_{VM,systolic} - \varepsilon_{VM,diastolic} \quad (2)$$

where the von Mises strain is a strain invariant defined by:

$$\varepsilon_{VM} = \left[\frac{(\varepsilon_I - \varepsilon_{II})^2 + (\varepsilon_{II} - \varepsilon_{III})^2 + (\varepsilon_I - \varepsilon_{III})^2}{2} \right]^{1/2} \quad (3)$$

and ε_I , ε_{II} and ε_{III} are the principal strains.

Note that the cyclic strain dynamical components (*i.e.*, the difference between systolic and diastolic values of the von Mises strain) rather than absolute strain, are believed to play a role in biological remodeling [32].

All calculations were performed using a SGI Origin 2000 computer equipped with 4 processors and 6 GB of RAM (approximately 1.2 GB were needed for this computation).

4. Results

To gain insight into the common features in human carotid bifurcation cyclic strain patterns, we first examined the idealized model (see Figure 7) along its inner wall (*i.e.*, the endothelial layer). The cyclic strain amplitudes in this model varied in a nearly linear fashion from 2–3%

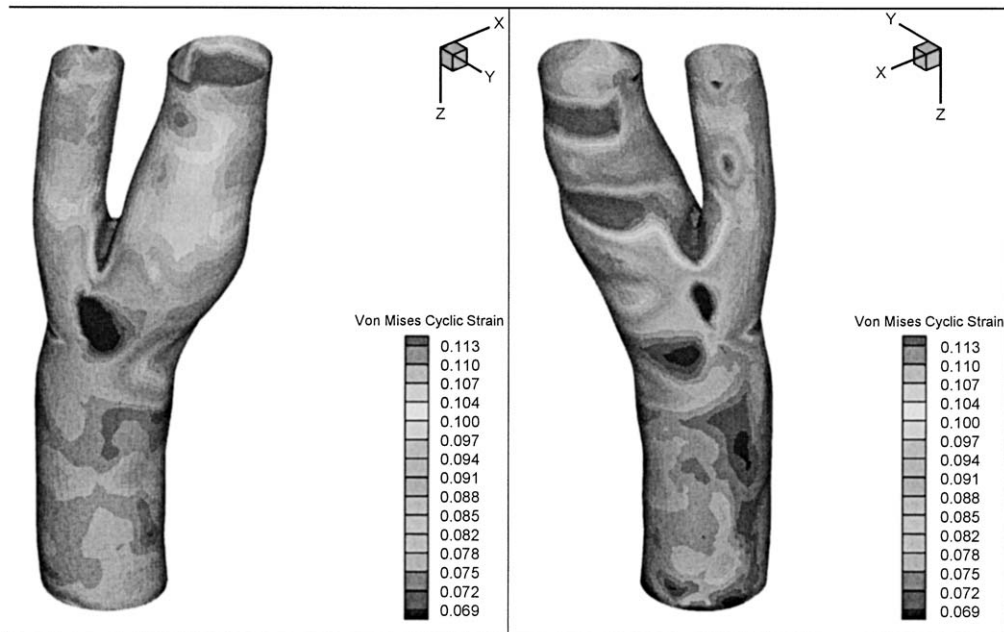


Figure 8. Von Mises cyclic strain distribution in healthy volunteer model NV1. Cyclic strain is computed as the difference between systolic and diastolic strain.

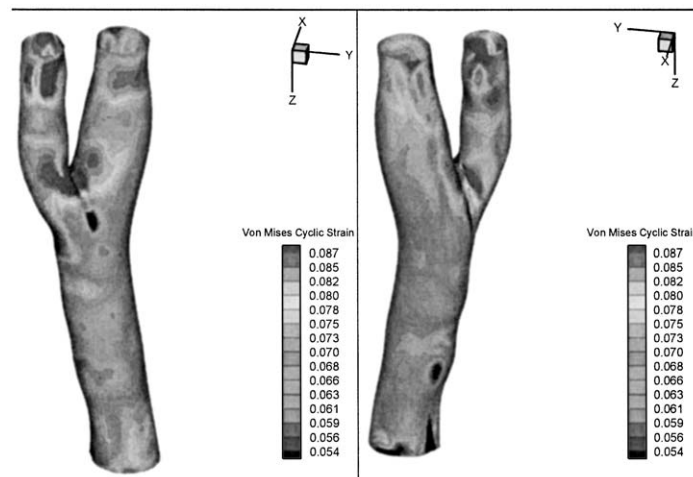


Figure 9. Von Mises cyclic strain distribution in healthy volunteer model NV2. Cyclic strain is computed as the difference between systolic and diastolic strain.

on the outer wall of the artery (data not shown) up to 5–7% on the inner wall (see Figure 7). Strain amplitudes are slightly smaller downstream of the carotid sinus, but the differences are rather small. Significant variations in cyclic strain amplitude are confined to the vicinity of the bifurcation. The wall opposite to the flow divider of the external carotid (the common-external adjoining wall) and the carotid apex, both common sites of early inflammation, as well as immediately distal to the carotid bulb, a site of late stage inflammation, are seen to experience the highest cyclic strain of 6–7% (vs. 4–5% elsewhere on the inner wall of the bifurcation).

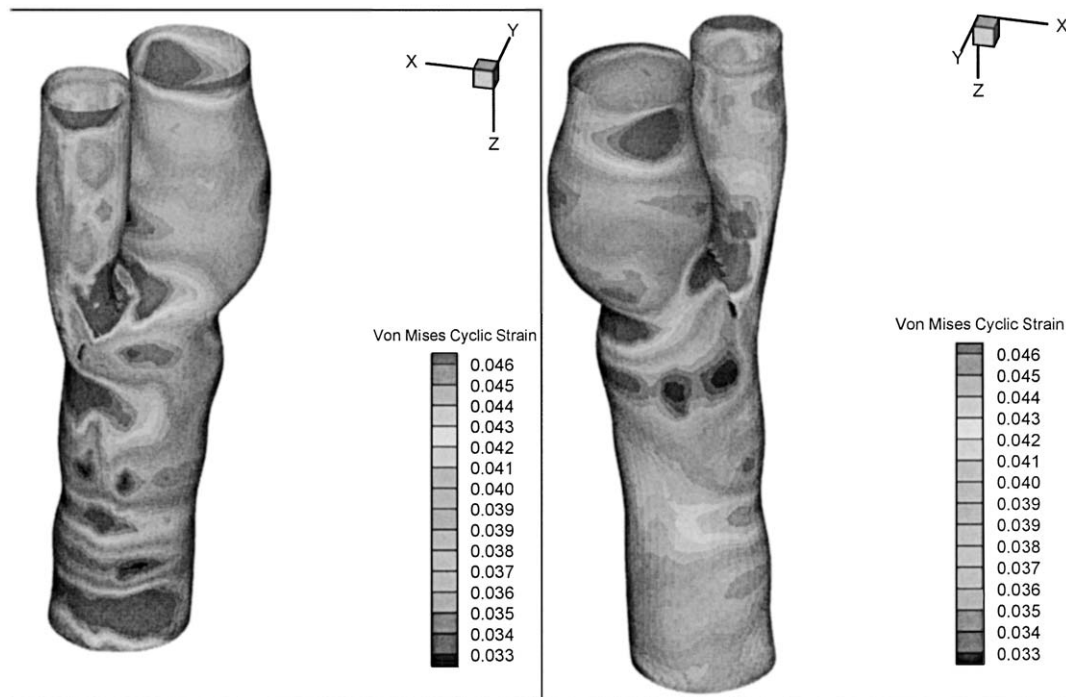


Figure 10. Von Mises cyclic strain patterns in healthy volunteer model NV3. Cyclic strain is computed as the difference between systolic and diastolic strain.

In order to investigate the importance of subject-specific anatomical features, we next examined the cyclic strain distributions in the realistic carotid bifurcation models from three healthy volunteers NY1-NY3 as shown in Figures 8–10, respectively. A common feature seen in all three models is that the levels of cyclic strain are highest at the apex, namely 14%, 11% and 6%, respectively, in the healthy-volunteer models of NY1, NY2, and NY3. A second area of high cyclic strain in all the geometries, although of smaller magnitude, is at the external-common adjoining wall (NY1: 11%, NV2: 9%, NV3: 5%). A region of elevated cyclic strain (12%) unique to NY1 appears between the internal carotid artery bulb and the apex (see Figures 1 and 4 for definition). Another region of elevated cyclic strain ($\sim 5\%$) is visible immediately proximal to the carotid bulb in NV3. NY3 also shows several patches of high cyclic strain in the common carotid artery that are absent in NV1 and NY2. In all the geometries (except the external carotid artery of NV1), there are localized regions of high cyclic strain at the ending of the internal and external carotid arteries immediately proximal to where the 10% axial stretch boundary conditions are applied; these are likely artifacts resulting from the proximity of the applied loads.

To study the effect of inhomogeneity in the arterial morphology and composition on the induced cyclic strain patterns, we next examined 2-D models with intra-plaque material properties distributed according to histology. Four specimens were analyzed, which contained different combinations of lipid core, arterial wall, fibrous plaque, and calcification (see Figures 11). These models correspond to slices at different locations on the common carotid and internal carotid arteries (see Section 2.3).

As evident in the Figure 11, the patient models exhibited a generally low cyclic strain, in the range of 4% or lower, both in the common carotid and proximal internal carotid arteries. This

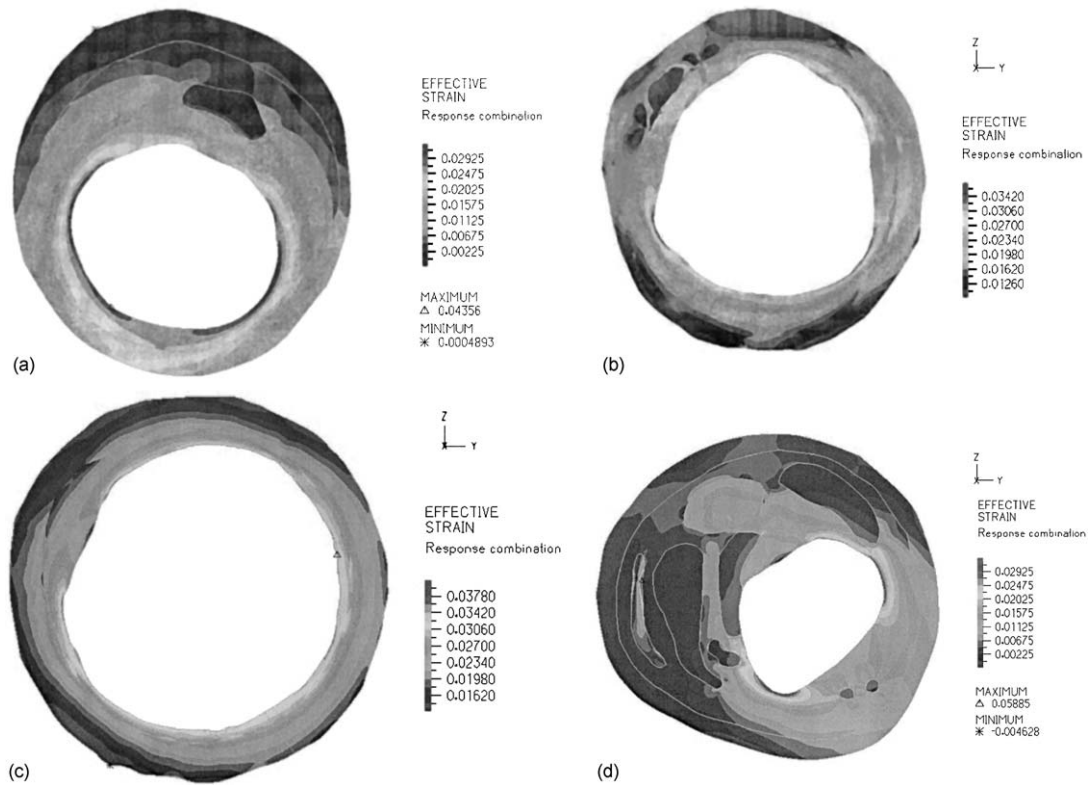


Figure 11. Von Mises cyclic strain patterns in the 2-D histology-derived models. Panels a–d correspond to finite-element models shown in panels a–d of Figure 6, respectively.

behavior is consistent with the arterial stiffening expected in diseased carotid bifurcations. The lipid pool region, however, can experience cyclic strain magnitudes as high as 11% (see Figures 11b and 6b). This is conceivable as lipid is characterized as a rubbery material that can easily deform to an optimum shape to minimize the stress/strain energy. In the extra-lipid areas, the highest cyclic strain lies in the shoulder regions of the plaque, on both sides of the lipid pool, and along the inner edge of the artery, which is opposite to the lipid pool region (see Figure 11b). This area, called fibrous cap, greatly contributes to the loss of biomechanical stability of the plaque. Due to its proximity to the applied pressure, the fibrous plaque region tends to sustain higher cyclic strains than the rest of the arterial wall, even though as previously supplied Mooney-Rivlin parameters indicate, the fibrous plaque is actually stiffer than arterial wall. This would tend to favor fatigue and rupture in these regions, a problem potentially compounded by the stimulation of MMP production by resident macrophages [11]. In models that lack lipid-pool regions, the cyclic strain varied in a nearly linear fashion from its maximum on the lumen boundary decreasing towards the outer boundary of the artery (see Figures 11a and 11c).

5. Discussion

The cyclic strain levels observed in our idealized, healthy and diseased carotid bifurcation models compare favorably with the corresponding distensibility levels detected clinically.

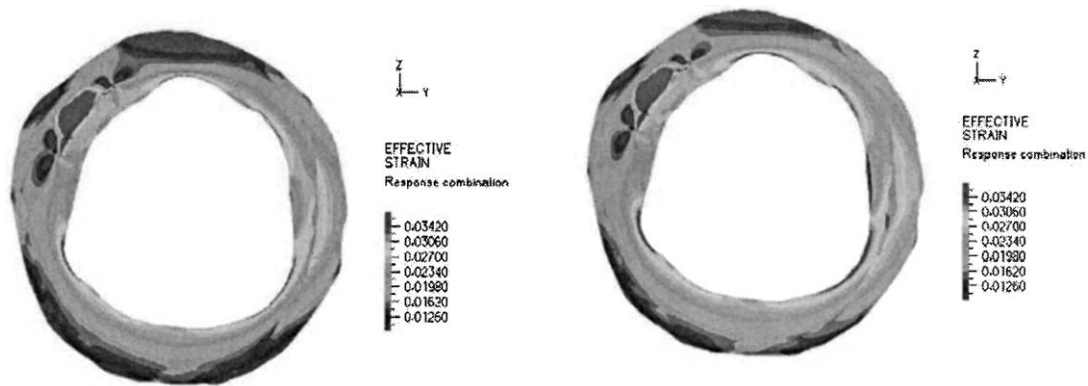


Figure 12. Comparison of Von Mises cyclic strain patterns in the 2-D histology-derived models without (left panel) and with residual strains (model with lipid pool).

Non-invasive measurements by Van Merode *et al.* [33] reveal distensibility values of $\sim 5\%$ in older volunteers (ages 50–60) and $\sim 11\%$ in younger volunteers (ages 20–30) in the common carotid. Specifically, the values detected in our idealized models were approximately 5% and circumferentially uniform over the inner wall of the common carotid. The subject-specific healthy models, however, exhibited higher values of cyclic strain, in the range of 5% to 8% in the common carotid. Due to the geometric complexity of the carotid bifurcation, it is not surprising that at areas of curvature and sharp intersections (*e.g.* the apex), the strain field is non-uniform. This is expected due to stress (and subsequently strain) concentrations arising there [23].

Schwenke and Carew [34] inspected the permeability of arterial branch sites in the healthy rabbit aorta and showed that such sites have a permeability that is on the order of four times higher than that of non-branching regions. Friedman *et al.* [21] also noted the increase in intimal permeability in regions of high wall shear stress and hypothesized that since albumin uptake is enhanced by shear, it is possible that other chemical reactions are mediated by high shear, but did not attempt to link this to intimal thickening. It is more likely, given the substantial amount of experimental evidence that links cyclic strain to EC proliferation, that the enhanced permeability occurs from ‘leaky cell junctions’ [14] during EC mitosis enhanced by high cyclic strain as is suggested by our results.

Whereas the earlier results of Friedman *et al.* [21] attribute the increased permeability to high shear stress, our results suggest an alternative explanation, linking high cyclic strain to enhanced permeability via ‘leaky cell junctions’. This is apparent at the carotid apex, which is a branch site with higher permeability [34] and experiences cyclic strain levels of $\sim 7\%$ in the idealized model and up to 11% in the anatomically realistic models of healthy carotid bifurcation. This observation, along with high levels of cyclic strain in the adjoining wall of the external-common carotid, support the possible role of cyclic strain in atherogenesis, since these two locations were also observed as regions of early atherosclerotic inflammation [20,21]. This is further supported by the results of Li *et al.* [13] who showed that cyclic strain increases EC proliferation and established that there exists an optimal cyclic strain range for EC proliferation ($<6.4\%$ vs. 6–11% observed in our idealized and realistic models), which if exceeded dampens the proliferative response.

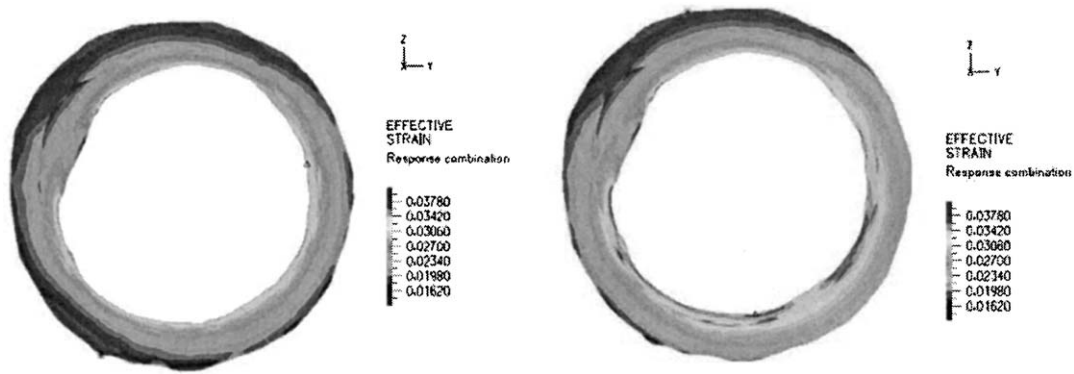


Figure 13. Comparison of Von Mises cyclic strain patterns in the 2-D histology-derived models without (left panel) and with residual strains (model with no lipid pool).

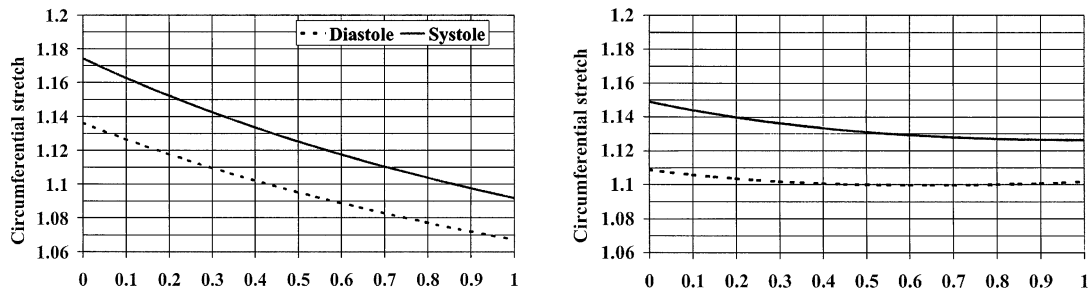


Figure 14. The effect of residual stresses on the strain field across the thickness of an axisymmetric cylindrical artery. The x -axis is plotted as a function of normalized thickness, with “0” being along the inner wall surface. The left graph illustrates the strain at systole and diastole without the inclusion of residual stresses, the right graph with. Note that even though the strain field is altered (more uniform when residual stresses are included), the magnitude of the cyclic strain (obtained as the difference between the solid and dashed lines) is nearly identical in the two cases.

A striking degree of uniformity was found in the strain amplitudes over much of the wall in the idealized model (Figure 7). The anatomically realistic models, on the other hand, showed significant variations in cyclic strain around the circumference (see Figures 8–10). This finding must be viewed with caution, however, keeping in mind that the nonuniformity of strain around the circumference is very sensitive to even small errors in wall thickness that are likely to arise due to limited resolution of MR images [27].

A potentially more important concern is how the inclusion of residual stresses would affect the cyclic strain patterns observed here. Previous researchers have shown that residual stresses can exert a significant effect on the stress field in an artery [22,35,36]. An excised arterial segment typically opens up when cut at one point along the circumference, eventually to a steady state opening angle. This suggests that in its closed configuration, the artery is not in a stress-free state when the transmural pressure is zero [36], but rather that the circumferential stresses are generally compressive along the inner wall and tensile along the outer wall. Lack of an unambiguous means to introduce residual strains, even in the idealized model, makes it nontrivial to assess their effects, or lack thereof, on the cyclic strain patterns. However, since the excised slices of the diseased artery were available to us immediately after they were cut in the endarterectomy procedure, we utilized them for a fairly rigorous assessment of residual strain in those models. Using FEM utilities available in ADINA, a technique was devised to

bring together the two cut ends of the slice. Specifically, ‘truss elements’ were introduced between corresponding points on the two ends of the excised slices. Using a thermal load, the truss elements were then shrunk so that the ‘gap’ was completely closed, giving rise to strain patterns that mimicked the residual strains. After implementing a closed specimen with the residual strains incorporated, a pressure loading was applied as a boundary condition on the interior boundary of the plaque slice¹. The applied systolic/diastolic pressures in the artery were then calculated from patient-specific MRI-based 3-D FEM hemodynamic simulations [19]. As evident in Figures 12 and 13, the magnitude of the cyclic strain is hardly affected by the inclusion of residual strains, especially in the model that includes a lipid pool. In other words, the dynamic component of strain remains generally unaffected, even though the absolute magnitude of stress or strain in the artery is changed by inclusion of residual stresses (producing smaller radial stress/strain gradients at normal arterial pressure, as typically found in normal healthy arteries). This observation is consistent with the simple case of a cylindrical artery with and without residual strains (see Figure 14). Moreover, *in vitro* experiments tend to suggest that the ‘dynamic’ component of strain is most likely to elicit a cellular response, because the resident cells will eventually yield to the local mean level of wall strain. It has been observed that bio-modeling and remodeling occurs in a manner consistent with the patterns of strain variations [32], rather than mean strain levels. Furthermore, endothelial cells support virtually none of the load on the arterial wall [37], and likely adapt to the mean strain level, responding only to dynamic changes in strain levels.

6. Concluding remarks

There are many experimental results, both *in vivo* and *in vitro* that favor a correlation between cyclic strain and atherogenesis, based on observations that implicate high cyclic strain to the stimulation of endothelial and smooth muscle cells. Several geometries were used in this study to model the human carotid bifurcation, namely a 3-D, idealized geometry, 3-D anatomically realistic subject-specific geometries based on *in vivo* images of three healthy volunteers, and finally 2-D models based on histology-derived patient-specific anatomy and intra-plaque components. The adjoining wall of the external-common carotid and the carotid apex, both frequent sites of early inflammation were seen to experience relatively high cyclic strains. An area of elevated cyclic strain amplitude is also detected immediately distal to the bulb, suggesting that cyclic strain may play a role in that region as well.

The subject-specific healthy models exhibited slightly higher values of cyclic strain. Local secondary geometric features led to relatively non-uniform strain fields. The patient models based on histology exhibited a generally low cyclic strain in the range of 4% or lower, both in the common carotid and proximal internal carotid arteries, a behavior consistent with the arterial stiffening expected in diseased carotid bifurcations.

The idealized model did not provide conclusive results indicating the existence of correlations between high cyclic strain levels and common sites of atherosclerosis, with cyclic strain values being ~5% in most areas, and 6–7% in susceptible areas. The results in the anatomically realistic models, however, showed that the carotid apex and adjoining wall of the external-common carotid, both sites of early atherosclerotic inflammation, tend to exhibit high

¹It is worth noting that the geometries of 2-D models presented in Figure 11 were created in the same manner, except that in those models the post-closure strains were released prior to applying the pressure loading, while keeping the geometry closed.

cyclic strain. High cyclic strain has been implicated in stimulation of endothelial and smooth muscle cells. On the other hand, the carotid bulb, another common site of atherosclerosis, appears to be a region of moderate cyclic strain amplitudes and is thus not explained by our hypothesis. This reinforces the notion that arterial disease is multi-factorial and cannot be attributed to one single mechanical (or biochemical) factor.

Acknowledgements

Support from the National Heart, Lung, and Blood Institute (HL 61794) is gratefully acknowledged.

References

1. T.J. Reape and P.H. Groot, Chemokines and atherosclerosis. *Atherosclerosis* 147 (1999) 213–225.
2. Q. Capers, R.W. Alexander, P. Lou, H. De Leon, J.N. Wilcox, N. Ishizaka, A.B. Howardt and W.R. Taylor, Monocyte chemoattractant protein-1 expression in aortic tissues of hypertensive rats. *Hypertension* 30 (1997) 1397–1402.
3. M.J. Jiang, Y.J. Yu, Y.L. Chen, Y.M. Lee and L.S. Hung, Cyclic strain stimulates monocyte chemotactic protein-1 mRNA expression in smooth muscle cells. *J. Cell Biochem.* 76 (1999) 303–310.
4. D.L. Wang, B.S. Wung, Y.J. Shyy, C.F. Lin, Y.J. Chao, S. Usami and S. Chien, Mechanical strain induces monocyte chemotactic protein-1 gene expression in endothelial cells. Effects of mechanical strain on monocyte adhesion to endothelial cells. *Circ. Res.* 77 (1995) 294–302.
5. B.S. Wung, J.J. Cheng, Y.J. Chao, J. Lin, Y.J. Shyy and D.L. Wang, Cyclical strain increases monocyte chemotactic protein-1 secretion in human endothelial cells. *Am. J. Physiol.* 270 (1996) H1462–H1468.
6. G.C. Cheng, W.H. Briggs, D.S. Gerson, P. Libby, A.J. Grodzinsky, M.L. Gray and R.T. Lee, Mechanical strain tightly controls fibroblast growth factor-2 release from cultured human vascular smooth muscle cells. *Circ. Res.* 80 (1997) 28–36.
7. A.W. Clowes, M.A. Reidy and M.M. Clowes, Mechanisms of stenosis after arterial injury. *Lab. Invest.* 49 (1983) 208–215.
8. C.L. Jackson and M.A. Reidy, Basic fibroblast growth factor: its role in the control of smooth muscle cell migration. *Am. J. Pathol.* 143 (1993) 1024–1031.
9. V. Lindner and M.A. Reidy, Expression of basic fibroblast growth factor and its receptor by smooth muscle cells and endothelium in injured rat arteries. An en face study. *Circ. Res.* 73 (1993) 589–595.
10. I.J. Mason, The ins and outs of fibroblast growth factors. *Cell* 78 (1994) 547–552.
11. R.T. Lee, C. Yamamoto, Y. Feng, S. Potter-Perigo, W.H. Briggs, K.T. Landschulz, T.G. Turi, J.F. Thompson, P. Libby and T.N. Wight, Mechanical strain induces specific changes in the synthesis and organization of proteoglycans by vascular smooth muscle cells. *J. Biol. Chem.* 276 (2001) 13847–13851.
12. J.M. Lemire, K.R. Braun, P. Maurel, E.D. Kaplan, S.M. Schwartz and T.N. Wight, Versican/Pg-M isoforms in vascular smooth muscle cells. *Arterioscler. Thromb. Vasc. Biol.* 19 (1999) 1630–1639.
13. G. Li, I. Mills and B. Sumpio, Cyclic strain stimulates Endothelial cell proliferation: Characterization of strain requirements. *Endothelium* 2 (1994) 177–181.
14. S. Weinbaum, G. Tzenghai, P. Ganatos, R. Pfeffer and S. Chien, Effect of cell turnover and leaky junctions on arterial macromolecular transport. *Am. J. Physiol.* 248 (1985) H945–H960.
15. S.J. Lin, K.M. Jan, S. Weinbaum and S. Chien, Transendothelial transport of low density lipoprotein in association with cell mitosis in rat aorta. *Arteriosclerosis* 9 (1989) 230–236.
16. S. Chien, S.J. Lin, S. Weinbaum, M.M. Lee and K.M. Jan, The role of arterial endothelial cell mitosis in macromolecular permeability. *Adv. Exp. Med. Biol.* 242 (1988) 59–73.
17. B.I. Tropea, S.P. Schwarzacher, A. Chang, C. Asvar, P. Huie, R.K. Sibley and C.K. Zarins, Reduction of aortic wall motion inhibits hypertension-mediated experimental atherosclerosis. *Arterioscler. Thromb. Vasc. Biol.* 20 (2000) 2127–2133.
18. D.N. Ku, D.P. Giddens, C.K. Zarins and S. Glagov, Pulsatile flow and atherosclerosis in the human carotid bifurcation. Positive correlation between plaque location and low oscillating shear stress. *Arteriosclerosis* 5 (1985) 293–302.

19. M.R. Kaazempur-Mofrad, A.G. Isasi, Y.F. Younis HF, R.C. Chan, D.P. Hinton, G. Sukhova, G.M. LaMuraglia, R.T. Lee and R.D. Kamm, Diseased Carotid Bifurcation fluid mechanics based on in vivo magnetic resonance images: Relationship of Shear Stress an Inflammation. *Annals Biomed. Engng.* (2003). Submitted.
20. N. Masawa, S. Glagov and C.K. Zarins, Quantitative morphologic study of intimal thickening at the human carotid bifurcation: I. Axial and circumferential distribution of maximum intimal thickening in asymptomatic, uncomplicated plaques. *Atherosclerosis* 107 (1994) 137–146.
21. M.H. Friedman, O.J. Deters, C.B. Bargeron, G.M. Hutchins and F.F. Mark, Shear dependent thickening of the human arterial intima. *Atherosclerosis* 60 (1986) 161–171.
22. A. Delfino, N. Stergiopulos, J.E. Moore Jr. and J.J. Meister, Residual strain effects on the stress field in a thick wall finite-element model of the human carotid bifurcation. *J. Biomech.* 30 (1997) 777–786.
23. R.S. Salzar, M.J. Thubrikar and R.T. Eppink, Pressure-induced mechanical stress in the carotid artery bifurcation: a possible correlation to atherosclerosis. *J. Biomech.* 28 (1995) 1333–1340.
24. B.K. Bharadvaj, R.F. Mabon and D.P. Giddens, Steady flow in a model of the human carotid bifurcation. Part I—flow visualization. *J. Biomech.* 15 (1982) 349–362.
25. A. Delfino, *Analysis of Stress Field in a Model of the Human Carotid Bifurcation*. Ph.D. Thesis, Department of Physics, Ecole Polytechnique Federale de Lausanne, Lausanne, Switzerland (1996) 235 pp.
26. K.J. Bathe, *Finite Element Procedures*. Englewood Cliffs, N.J.: Prentice Hall (1996) 1037 pp.
27. H.F. Younis, M.R. Kaazempur-Mofrad, R.C. Chan, A.H. Chau, D.P. Hinton, A.G. Isasi, L.A. Kim and R.D. Kamm, A numerical study of carotid artery wall and fluid mechanics based on in vivo magnetic resonance images of healthy volunteers. *Biomech. Model. Mechanobiology* (2003). In press.
28. Y.C. Fung, K. Fronek and P. Patitucci, Pseudoelasticity of arteries and the choice of its mathematical expression. *Am. J. Physiol.* 237 (1979) H620–H631.
29. L. Lilly, *Pathophysiology of Heart Disease*. Baltimore: Lippincott Williams & Wilkins (1998) 401 pp.
30. H.M. Loree, A.J. Grodzinsky, S.Y. Park, L.J. Gibson and R.T. Lee, Static circumferential modulus of human atherosclerotic tissue. *J. Biomech.* 27 (1994) 195–204.
31. I.H.M. Loree, B.J. Tobias, L.J. Gibson, R.D. Kamm, D.M. Small and R.T. Lee, Mechanical Properties of model atherosclerotic lesion lipid pools. *Arterioscl. Thromb.* 14 (1994) 230–234.
32. R. Huiskes, R. Ruimerman, G.H. van Lenthe and J.D. Janssen, Effects of mechanical forces on maintenance and adaptation of form in trabecular bone. *Nature* 405 (2000) 704–706.
33. T. Van Merode, P.J. Brands, A.P. Hoeks and R.S. Reneman, Different effects of aging on elastic and muscular arterial bifurcations in men. *J. Vasc. Res.* 33 (1996) 47–52.
34. D.C. Schwenke and T.E. Carew, Initiation of atherosclerotic lesions in cholesterol-fed rabbits. II. Selective retention of LDL vs. selective increases in LDL permeability in susceptible sites of arteries. *Arteriosclerosis* 9 (1989) 908–918.
35. C.J. Chuong and Y.C. Fung, On residual stresses in arteries [published erratum appeared in *J. Biomech. Engng.* 112 (1990) 249]. *J. Biomech. Engng.* 108 (1986) 189–192.
36. Y.C. Fung, What are the residual stresses doing in our blood vessels? *Ann. Biomed. Engng.* 19 (1991) 237–249.
37. J.D. Humphrey, Mechanics of the arterial wall: review and directions. *Crit. Rev. Biomed. Engng.* 23 (1995) 1–162.